

Optimizing CMOS-compatible, superconducting Titanium Nitride Resonators: Deposition Conditions and Structuring Processes

S. J. K. Lang*,¹ A. Schewski*,¹ I. Eisele,^{1,2} J. Weber,¹ C. Moran Guizan,¹ Z. Lou,³ M. Singer,³ B. Schoof,³ M. Tornow,^{1,3} T. Mayer,¹ D. Zahn,¹ R. N. Pereira,¹ and C. Kutter^{1,2}

(*These authors contributed equally to this work and are listed in alphabetical order.)

¹*Fraunhofer Institute for Electronic Microsystems and Solid State Technologies EMFT, Munich, Germany*

²*Center Integrated Sensor Systems (SENS), Universität der Bundeswehr München, Munich, Germany*

³*Technical University of Munich, TUM School of Computation, Information and Technology, Department of Electrical Engineering, Garching, Germany*

(*Electronic mail: alexandra.schewski@emft.fraunhofer.de)

(*Electronic mail: simon.lang@emft.fraunhofer.de)

(Dated: 3 March 2026)

We report on the fabrication and characterization of superconducting coplanar waveguide (CPW) resonators based on titanium nitride (TiN) thin films deposited on 200 mm diameter high-resistivity Si(100) substrates. We systematically investigate how deposition conditions, dry-etch power and in-situ resist strip temperature affect morphology, superconducting properties and dielectric losses. By tuning reactive sputtering conditions, three distinct preferred crystal orientations — (111), (200), and mixed are achieved. Our results demonstrate that all films exhibiting similar minimal two-level system (TLS) losses, with TiN111 exhibit the lowest median TLS losses δ_{TLS} , and greater robustness against reoxidation. The applied structuring process, in contrast, had a far greater influence on the TLS loss than the crystal orientation of the TiN film and, consequently, the intrinsic material properties of the superconducting layer. The lowest TLS losses for all TiN depositions were achieved with a low power etch and low temperature resist strip. An additional buffered oxide etch (BOE) treatment could remove high-loss interfacial oxides at the metal-air (MA) and substrate-air (SA) interface and recover the etch-induced TLS losses. Consequently, TiN resonators exhibiting δ_{TLS} values as low as 9.67×10^{-7} were realized. The corresponding median low-power loss, δ_{LP} , amounts to 11.04×10^{-7} , which translates to an internal quality factor approaching one million. These findings highlight the critical role of process induced oxide formation at the MA and SA interfaces in limiting the performance of TiN resonators and provide a scalable, low-loss process compatible with industry-grade 200 mm CMOS qubit fabrication workflows.

I. INTRODUCTION

Quantum computing promises to tackle computational tasks that lie beyond the reach of classical machines operating within a practical timeframe. For example, Shor's algorithm enables efficient factorization of large integers into primes¹, and Grover's algorithm facilitates the rapid search of unstructured databases². One of the most promising hardware platforms for realizing large-scale quantum processors is based on superconducting qubits. These qubits are lithographically-defined superconducting circuits typically fabricated from aluminium, titanium nitride (TiN), as well as niobium on silicon (Si) or sapphire substrates. The use of Al and TiN enables compatibility with CMOS-style fabrication tools and supports scaling to large qubit counts^{3,4}. However, executing genuinely useful quantum algorithms in multi-qubit systems requires exceedingly low error rates. When the error rates for single- and two-qubit gates are reduced to the order of about 0.1% per operation, fault-tolerant quantum error-correction schemes become feasible—enabling logical qubits to be encoded across many physical qubits, and thereby allowing significantly more complex quantum circuits to execute reliably¹. A persistent challenge in superconducting platforms is that, at low powers, both qubit coherence and quality of microwave resonators are often limited by energy loss into parasitic two-level systems

(TLS) residing at interfaces or in bulk dielectric materials⁵. Coplanar waveguide (CPW) resonators provide an ideal platform for studying these TLS. When combined with electromagnetic participation-ratio models, their quality factors allow quantitative links between changes in the fabrication process and distinct loss channels, even in cases where fabrication variations couple to multiple loss mechanisms simultaneously.

Titanium nitride (TiN) is a key material for such resonators. It has excellent superconducting properties, it is thermally and mechanically robust and compatible with standard CMOS-style fabrication processes, making it especially well-suited for large-scale manufacturing. Although TiN resonators have been extensively studied in prior work⁶⁻¹², a remaining gap lies in the systematic assessment and demonstration of how individual fabrication steps affect resonator quality factors for realistic geometries. In this work we aim to address this gap by analyzing how various process parameters influence resonator performance. Importantly, we use identical resonator geometries across all processing conditions so that the participation ratios remain constant and any changes in quality factor can be attributed to processing rather than geometric variation.

The processes under detailed analysis are:

- TiN sputtering with reproducible films of different crystal orientation.
- Dry etching of resonators at high and low power.

- In-situ resist stripping at high and low power.
- Wet etching as a post processing surface etching technique.

II. METHODS

A. Chip Layout

The chip layout used throughout this study can be seen in Figure 1. Each chip incorporates nine quarter-wave ($\lambda/4$) resonators, all coupled to a single common feedline for simultaneous signal input and extraction within a single frequency sweep. The coupling to the feedline was designed to be 0.36 MHz ($Q_{\text{ext}} = 5e5$) for all of the resonators. The resonators themselves are implemented using a coplanar waveguide (CPW) geometry, featuring a central conductor width of $w = 10 \mu\text{m}$ and a gap to the ground planes of $g = 6 \mu\text{m}$. On each chip, the resonators are spaced 200 MHz apart in frequency. To cover the full frequency range of 4–10.4 GHz, four distinct chips were designed, each spanning a specific subset (4–5.6 GHz, 5.6–7.2 GHz, 7.2–8.8 GHz and 8.8–10.4 GHz) of the range. The design also includes vortex-pinning holes around the CPW lines to minimize flux trapping¹³.

B. Fabrication

For the fabrication of the chips whose layout is describe in Section II A 200 mm diameter Si(100) wafers with a resistivity of $> 3500 \Omega\text{cm}$ are used as substrates.

A 180 s long clean in 1% diluted hydrofluoric acid (corrosive GHS05/toxic GHS06 etchant) is used to remove the native oxide and precondition the silicon surface.

The wafers are then transferred within 15 minutes to a sputter cluster tool Clusterline 200 from Evatec with a base pressure of $1 \cdot 10^{-8}$ mbar. After a preheating step a layer of 150 nm of TiN is reactively sputtered on the Si surface using three different reactive sputtering processes. The parameter sets for the

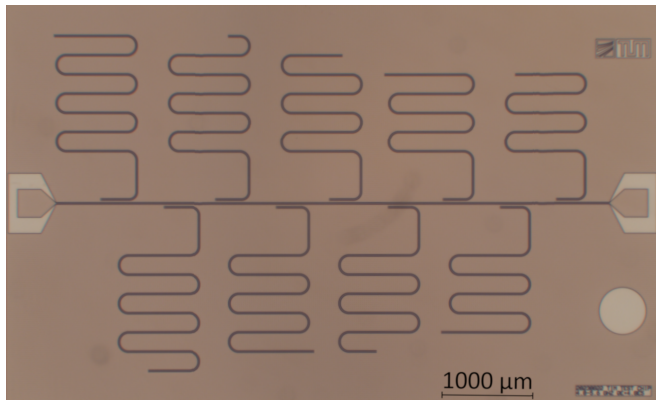


FIG. 1. Exemplary optical microscope image of chip fabricated and characterized within this study.

three tested conditions are summarized in Table I. They are a subset of process parameters variations tested in an earlier unpublished study and are chosen such that the resulting three films cover a wide range of different film properties in terms of crystallography and texture as will be discussed in detail in Sec III A 1).

Deposition is followed by SPA-3000 i4 Canon stepper photolithography. For structuring of the TiN resonators a MxP metal etch chamber and a ASP strip chamber available on the same Applied Materials P5000 mainframe are used. Two different dry etching recipes are tested whose parameters can be found in Table II and who are referred to as *high power* (HP) and *low power* (LP) etches.

Following the etching process, the photoresist is removed in-situ using an H_2O plasma strip. Two different temperatures are tested during this strip process: 250 °C (high temperature, HT) and 150 °C (low temperature, LT). Lastly, all samples undergo a chemical cleaning using CA25 from TechniClean (health hazard GHS07, flammable GHS02).

As further characterization is conducted at the chip level, the fabrication process at the wafer level was concluded by dicing.

To investigate the effects of surface oxidation, an additional surface treatment — a wet etching step using Honeywell ammonium fluoride etchant AF 875-125 LST (referred to as BOE; corrosive GHS05, toxic GHS06 HF-based etchant) — was tested at the chip level. To minimize reoxidation after this cleaning step one of the chips was cooled down within the next two hours (time coupling, t_c) for cryogenic characterization. All the other chips were also cooled down within 24 hours after the etching or BOE post treatment.

Table III summarizes all the combined process variations that will be analyzed within the course of this work. The last column also shows how many resonators are used for the characterization.

C. Room temperature characterization

Numerous room-temperature characterization methods are employed to monitor and evaluate the fabrication process. The uniformity and reproducibility of the TiN thin film deposition are assessed using wafer-scale sheet resistance measurements at nine points across the wafer, performed with a four-point probe test Omnimap instrument. The crystallinity and texture of the TiN thin film are analyzed using a $2\theta/\omega$ X-ray Diffraction (XRD) scan with a Rigaku Mini-Flex. Pseudo-Voigt peaks—a linear combination of Gaussian and Lorentzian functions—are fitted to the peaks in the $2\theta/\omega$

TABLE I. Parameters of reactive sputter processes tested for TiN film deposition.

Depo	Ar [sccm]	N ₂ [sccm]	Power [W]	Temp. [°C]
A	12	3.5	500	30
B	12	24	3000	400
C	16	50	6800	400

TABLE II. Parameters of TiN dry etch process (Power in Watts, flow rates in sccm, magnetic field in Gauss).

Etch	Power [W]	BCl ₃ [sccm]	Cl ₂ [sccm]	N ₂ [sccm]	B [Gauss]
HP	500	50	20	50	30
LP	70	0	80	40	40

TABLE III. Summary of all variations tested within the fabrication flow.

Depo	Etch	Resist strip	Wet etch	No. of Resonators
A	HP	HT	-	17
		LT	-	18
	LP	HT	-	18
		LT	-	17
B	HP	HT	BOE (with(out) tc)	16
		-	-	0
	LP	LT	BOE (without tc)	54
C	HP	HT	-	15
		LT	-	18
	LP	HT	-	9
		LT	-	18

scan to determine the peak positions and full width at half maximum (FWHM). The peak positions provide insights into the preferred crystal orientation and strain within the thin film, while the FWHM offers information about grain sizes when the grain size is smaller than the instrumental resolution¹⁴. A Helios 650 scanning electron microscope (SEM) is utilized to characterize the TiN thin films in terms of layer thickness and morphology. After structuring, the etching rim and the overetch depth into the substrate are also examined using SEM. Atomic force microscopy (AFM) measurements, performed with a Park Systems NX20, are used to evaluate the influence of the etching process on the substrate roughness by comparing the Si surface before TiN deposition and after etching. Finally, the oxidation of the Si surface is monitored using a spectral ellipsometer from SENTECH Instruments.

D. Cryogenic characterization

The measurements for critical temperature (T_c) of the produced TiN thin films were carried out on a kiutra system, which provides accurate temperature sweeps and enables to determine the residual resistance ratio (RRR) according to the equation:

$$RRR = \frac{R(300K)}{R(\text{just above } T_c)} \quad (1)$$

A smaller RRR value implies that the resistance right above T_c is comparable to the room temperature resistance. This means that the film under consideration has a low defect density. The cryogenic characterization of the resonators is done in a Bluefors dilution refrigerator and a cryostat from Qnu at

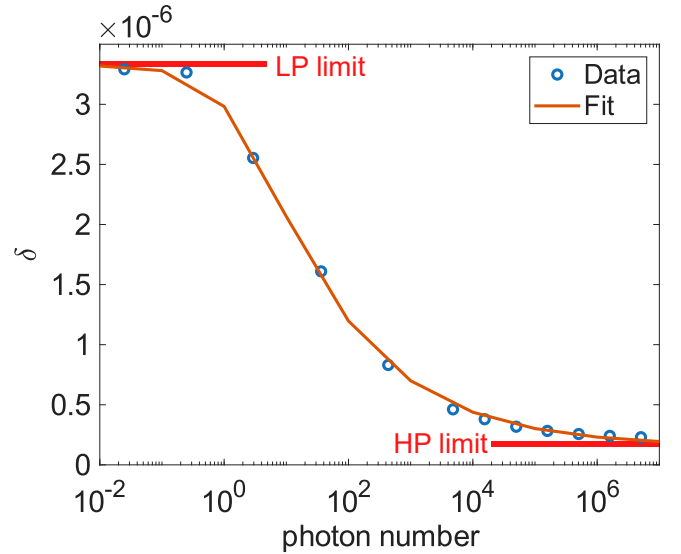


FIG. 2. Exemplary fit of Eq. (3) (orange) on the dielectric loss (blue) extracted of one resonator measured at $T < 25$ mK. The LP and HP limit are marked in red.

temperatures below $T < 25$ mK. The measurement process begins with identifying the resonance peaks through a coarse transmission sweep. Following this, the complex scattering parameter S_{21} is measured using a vector network analyzer (VNA)^{15,16}, which is designed to generate and analyze microwave signals. The internal quality factor Q_i is determined by fitting the measured data using the procedure outlined in Ref. 17. The excitation power of the VNA can be converted into the corresponding photon number $\langle n \rangle$ following the method described by A. Bruno et al. in Ref. 18. The internal quality factor is inversely related to the dielectric loss ($Q_i = 1/\delta$). TLS defects couple to the electromagnetic fields of the resonator and introduce dissipation and dephasing¹⁹. For high powers (δ_{HP}) the dielectric loss decreases as the TLS get saturated. For low powers (δ_{LP}) the TLS loss dominates such that δ_{TLS} can be extracted by the following simplified equation²⁰:

$$\delta_{TLS} = \delta_{LP} - \delta_{HP} \quad (2)$$

One resulting exemplary measurement of the material losses depending on $\langle n \rangle$ is shown in Figure 2. The data points describe a curve given by

$$\delta(\langle n \rangle) = \delta_{LP} \frac{1}{(1 + \langle n \rangle / n_c)^\beta} + \delta_{HP}, \quad (3)$$

under the assumption of a broad distribution of TLS in the continuum approximation and in the limit $T \rightarrow 0$. Here, n_c is the critical photon number and β is a fit parameter that characterizes how rapidly the TLS contribution decreases with increasing drive (see reference²⁰ and related TLS models).

Each resonator is analyzed individually, and the variation in δ_{TLS} and δ_{LP} is statistically evaluated using the interquartile range (IQR) and its median values, $\tilde{\delta}_{TLS}$ and $\tilde{\delta}_{LP}$ for multiple resonators.

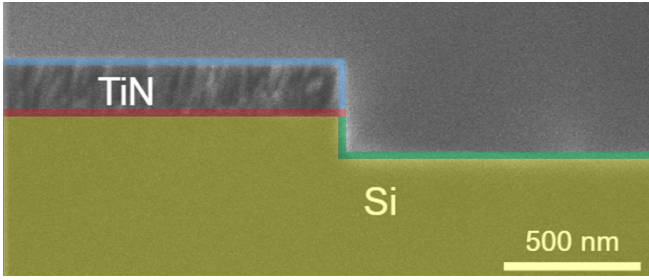


FIG. 3. SEM image of CPW resonator in cross sectional view with the dielectric regions contributing to TLS loss marked in yellow (Si), red (MS), blue (MA) and green (SA).

E. Electro-magnetic-participation-ratio model

For CPW resonators the electro-magnetic-participation-ratio model describes how TLS-related losses can be analyzed^{21,22}. A cross-section of a CPW resonator is shown in Fig. 3, where four dielectric regions i contributing to TLS loss are indicated: the bulk silicon substrate ($i = Si$, yellow), the metal–substrate interface ($i = MS$, red), the metal–air interface ($i = MA$, blue), and the substrate–air interface ($i = SA$, green). Each region has its own loss tangent δ_i . Depending on the resonator design, the so-called participation ratio p_i —defined as the fraction of the total electromagnetic energy stored (more precisely: the fraction of the energy stored in the electric field \vec{E} in a length element s , divided by the total energy per unit length E_{tot}) in region i , with thickness t_i and dielectric constant ϵ_i —can be varied^{5,23}. The participation ratio p_i is then defined by

$$p_i = \frac{t_i \epsilon_i}{E_{\text{tot}}} \int d\vec{s} |\vec{E}|^2, \quad (4)$$

The resulting δ_{TLS} is given as the sum of all loss tangent δ_i weighted with their respective participation ratio p_i according to the following equation:

$$\delta_{\text{TLS}} = p_{MA} \delta_{MA} + p_{MS} \delta_{MS} + p_{SA} \delta_{SA} + p_{Si} \delta_{Si} \quad (5)$$

Because the participation ratios depend sensitively on resonator geometry parameters like signal-line width, gap between signal and ground, film thickness and over-etch depth into the silicon substrate one can tailor p_i by design. The loss tangent δ_{TLS} can be determined experimentally by cryogenic measurements.

Disentangling the individual δ_i , however, is challenging: typically, the δ_i differ by orders of magnitude such that the influence of some loss region might not be resolved when the resonator is dominated by another loss. In the worst-case scenario, processes such as anisotropic trenching can couple simultaneously to multiple loss channels and, by altering the geometry, also change the participation ratios²⁴. HFSS simulations summarized in table IV show how the participation ratios for loss contributing regions i vary for expected overetch depths of ≤ 100 nm assuming a 2 nm dielectric layer thickness for the MA, SA and MS region.

TABLE IV. Simulated participation ratios of CPW resonators with 10 μm width and 6 μm gap for different trench depths.

Trench depth [nm]	p_{SA}	p_{MA}	p_{MS}	p_{Si}
0	$2.83 \cdot 10^{-4}$	$4.95 \cdot 10^{-5}$	$5.93 \cdot 10^{-4}$	0.907
50	$2.67 \cdot 10^{-4}$	$2.08 \cdot 10^{-5}$	$5.45 \cdot 10^{-4}$	0.905
100	$2.51 \cdot 10^{-4}$	$1.77 \cdot 10^{-5}$	$5.04 \cdot 10^{-4}$	0.903

TABLE V. Sheet resistance statistics on four wafers each for TiN films deposited using the parameters from Table III and resulting crystal orientations. Be aware that column five shows the maximum *pointwise* σ within the batch.

Depo	R_{\square} [Ω/sq]	Max σ wafer [%]	Max σ batch [%]	ρ [$\mu\Omega\text{-cm}$]	Crystal orientation
A	11.9	19.0	9.7	203	111
B	4.35	4.25	3.6	74	Mixed
C	4.7	4.0	2.0	65	200

III. RESULTS AND DISCUSSION

A. Room temperature characterization

1. TiN deposition characterization

For each of the three sputter processes (A, B, and C), four wafers are being deposited. The resulting twelve wafers are characterized using sheet resistance measurements to determine the uniformity and the reproducibility of the process. Table V summarizes the mean of all sheet resistances measured on the batch and its maximum standard deviation, as well as the maximum point-wise standard deviation over the entire batch. While process A done at lower temperatures shows a stronger nonuniformity, process B and C have a uniformity below 5% over one wafer as well as within the whole batch. The reduced uniformity may stem from the low power used for process A, which approaches the minimum threshold of the deposition chamber’s capabilities.

For each film the thickness d of the TiN layers is measured in a cross-sectional SEM image (like the one visible in Figure 6) and results together with the corresponding sheet resistance measurement in the resistivity ρ of the film according to $\rho = R_{\square} \cdot d$. While the films B and C have with $\rho = 74 \mu\Omega\text{-cm}$ and $\rho = 65 \mu\Omega\text{-cm}$ similar resistivities, film A shows a value of $203 \mu\Omega\text{-cm}$ that is around three times as large. To ensure that all the point-wise characterization (XRD, T_c etc.) of the TiN films and also all the measured resonators use the same TiN thickness of approximately 150 nm the measurement spots are chosen and the chips are picked accordingly from the wafer.

The XRD measurements of all three thin films are shown in Figure 4. Pseudo-Voigt profiles (indicated in black) are fitted to all of the occurring peaks to determine the peak positions and full width at half maximum (FWHM). The resulting FWHM values are annotated in Figure 4. The two peaks observed can be attributed to different orientations of the fabri-

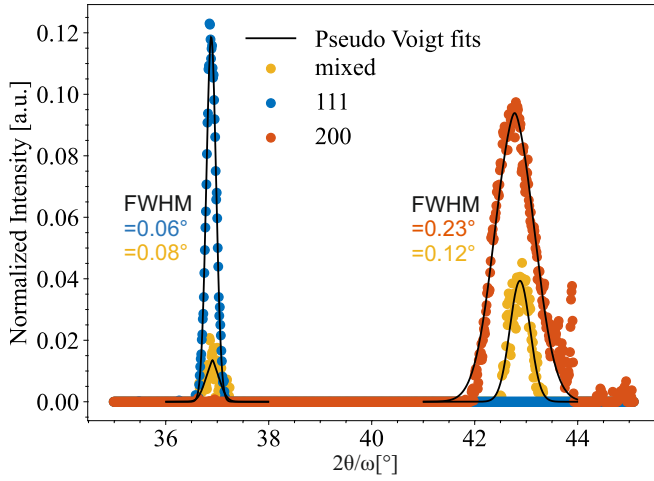


FIG. 4. XRD measurements of the different TiN depositions (A=111, B=mixed, C=200). The peaks at 42.5° and 36.5° correspond to different TiN crystal orientations: (200) and (111), respectively.

cated TiN film. The film sputtered using recipe A shows only one peak at 36.9°, which corresponds to the (111) plane of TiN. The shift of the peak position by +0.3° compared to the literature value^{25,26} might be attributed to (chemical) strain in the film. Since the $2\theta/\omega$ scan provides information only about out-of-plane lattice parameters, it can be concluded that the (111) orientation is the dominant out-of-plane crystal orientation of this film. Therefore, this film will be referred to as the TiN111 film from now on. The thin film resulting from recipe C shows no peak around 37° but exhibits a broader peak at 42.8° (with a shift of +0.2° with respect to the literature value^{25,26}, which might also be attributed to strain). This peak corresponds to the (200) plane of TiN. Hence, this film will be referred to as the TiN200 film. Recipe B results in a film where both peaks, and therefore both orientations, are present. This film will be referred to as TiNmixed. The peak heights of the TiNmixed film are substantially lower compared to the peaks of the other two films, in particular the (111) peak. Since all three films have the same thickness, this suggests that a larger portion of the TiNmixed film may be amorphous, with a particularly small amount of TiN111 grains. Amorphous films with some degree of short-range order contribute to XRD spectra only in cases of large film thicknesses¹⁴. It is possible that amorphous regions are also present in the TiN111 and TiN200 films for the same reason. If the peaks are broadened beyond the peak from the Si reference (as observed here), this indicates that the broadening cannot be explained solely by the XRD's instrumental resolution function. Instead, it must be attributed to either microstrain or reduced grain sizes¹⁴. Among the three films, the TiN111 film has the smallest FWHM, while the TiN200 film exhibits a FWHM that is nearly four times larger. The TiNmixed film shows intermediate grain sizes. From this, it can be concluded that the TiN111 film has either the lowest microstrain or the largest grain size, while the TiN200 film has the highest microstrain or the smallest grain size. Due to the inverse relationship between grain size and FWHM (given by

the Scherrer equation where $\text{grain size} \propto \frac{1}{\text{FWHM} \cdot \cos(\theta)}$), the grains in the TiN111 film may approximately be up to four times larger than those in the TiN200 film¹⁴. The XRD analysis indicates that the different deposition parameter sets produced three distinctly different TiN thin films. This diversity is beneficial for subsequent analysis, as it allows investigation of the influence of process parameters on the resulting dielectric losses across a wide range of film characteristics.

To better understand the texture of the films, Figure 5 shows high-resolution SEM images of all three films. The SEM images reveal fine grains (<40 nm) across all depositions. However, TiN111 films show larger, well-defined grains with pronounced broad grain boundaries, whereas the TiN200 film appears to have smaller grains with less notable grain boundaries. The TiNmixed film resembles the TiN200 film but includes small islands that resemble TiN111 grains. This observation aligns fully with the XRD results presented earlier and confirms that at least part of the peak broadening can be attributed to the grain size of the film.

2. TiN structuring characterization

Figure 6 shows TiN films after two different structuring processes have been applied, whose parameters are described in Table II. The influence of the strip process (here the HT strip) is not visible in the SEM images; its microscopic effects will be discussed below. The HP recipe produces steep, well-defined sidewalls. The plan view in the upper image shows a clean etching edge in the TiN and a straight overetch into the silicon. The lower image provides a cross-sectional view of the etching edge after cleaving, enabling measurement of the overetch depth into the silicon. All samples within this work exhibit an overetch depth in the range of 20–100 nm. In contrast, the LP etch results in sidewalls that appear rough and inhomogeneous, with no visible overetch into silicon, even for extended etch times. Instead, it seems that the TiN near the interface begins to be etched, resulting in a slight underetch. During the process, the parameters listed in Table II result in a DC bias on the susceptor where the wafer is positioned. The HP recipe generates a bias of 180 V (for 500 W), while the LP recipe produces a bias of only 17 V (for 70 W). This indicates that the kinetic energy of the particles impacting the etched regions is an order of magnitude higher for the HP etch compared to the LP etch. This explains the steep sidewalls observed in Figure 6 and the larger overetch into the silicon. Therefore, the HP etch can be categorized as a process with a strong physical component and noninfinite etch selectivity. The heavier decomposition products of BCl_3 are likely contributors to this physical component. The LP etch, on the other hand, is primarily a chemical etch process, as evidenced by its high selectivity to silicon and the rough appearance of the sidewalls. The roughness of these sidewalls can be attributed to differing chemical etch rates for grain boundaries and TiN grains. AFM measurements of the etched silicon surface support this explanation. The reference RMS value of a blank silicon wafer is 0.7 nm. The HP etch leaves the silicon surface with an RMS of 1.2 nm, while the LP recipe results in

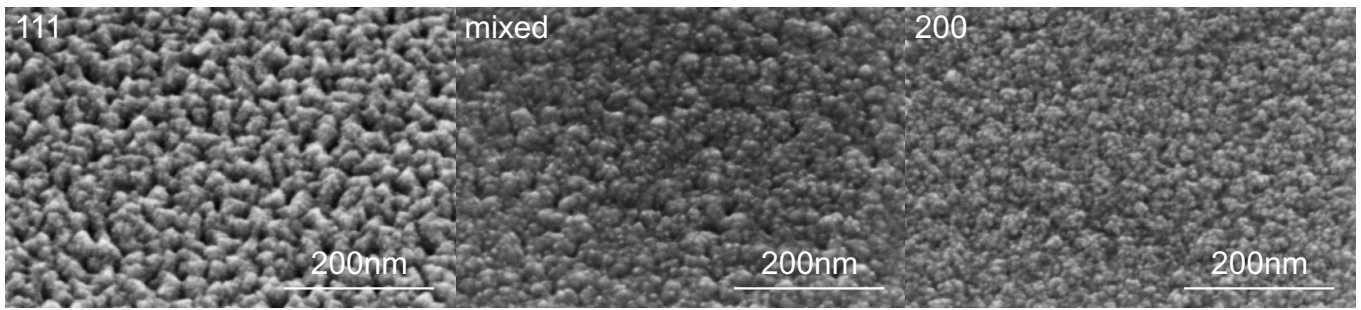


FIG. 5. SEM images of TiN deposited under different conditions to achieve preferential crystal orientations of (111), (200), and a mixture of both.

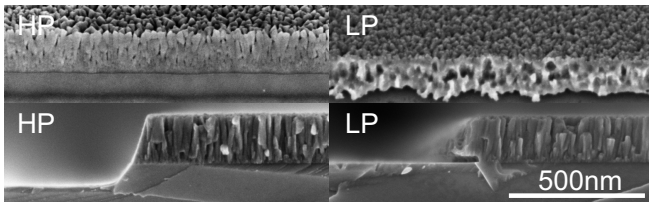


FIG. 6. SEM images of TiN111 etched with HP (left) and LP (right) etch processes in side view (upper images) and cross-sectional view after cleaving (lower images).

only slight roughening, leading to an RMS value of 0.8 nm.

The resist strip after etching is performed using water vapor plasma at different temperatures (LT and HT). During this step, the exposed silicon surface becomes oxidized. To investigate the oxidation behavior during the strip processes, spectral ellipsometry was used to measure the oxide thickness of three wafers using a Cauchy layer (with floating Cauchy coefficients N_0 , N_1). According to these measurements, an HF-dipped silicon wafer has an oxide thickness of 0.5 nm. After processing with the LT resist strip, the oxide thickness increases to 1.5 nm, and after the HT resist strip, it increases further to 3.2 nm. Although ellipsometer fits for such small layer thicknesses do not provide reliable absolute values, the increase in oxide thickness with higher temperature is certain. Furthermore, the increase in surface roughness observed in AFM measurements is likely to promote further oxidation. A similar behavior can be expected for the oxynitride formed on TiN, even though the TiN surface is exposed to oxygen only during the final moments of the resist strip process. TiN oxidizes to rutile TiO_2 at temperatures above 600°C in the absence of plasma²⁷, indicating that the formation of TiO_2 is thermodynamically favored over TiN. Since TiN forms an oxynitride layer on its surface even at room temperature, it is reasonable to assume that elevated temperatures and exposure to oxygen plasma during processing further increase the oxynitride thickness. As the resist strip is the final step in the process chain at elevated temperatures, we assume that no further oxidation occurs afterward. The following subsection will describe how this oxidation at the metal–air (MA) and substrate–air (SA) interfaces affects the energy losses in the resonators, and how removing these oxides using buffered ox-

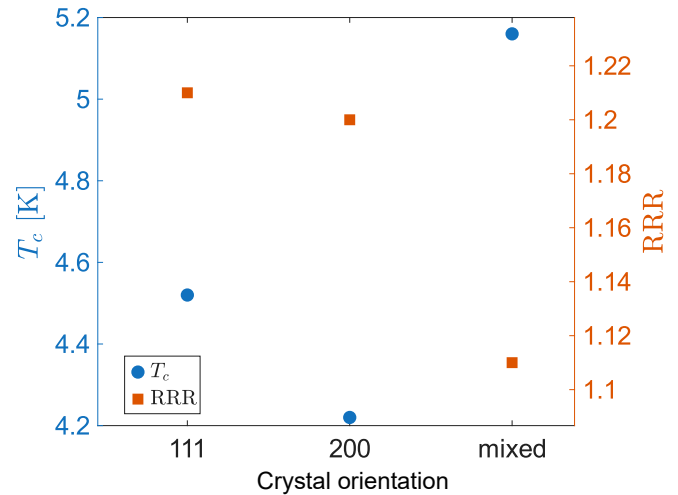


FIG. 7. Critical temperature (T_c) and RRR measured on films with different crystal orientations.

ide etch (BOE) changes those losses.

B. Superconducting properties and material losses

1. Influence of TiN material

The first part of the cryogenic characterization focuses on analyzing the influence of the TiN material on the RRR value, T_c , and the quality factor of the resonators. Figure 7 summarizes the first two of these three parameters. It is evident that all films have a residual resistance ratio (RRR) greater than 1, which is typical for materials with metallic behavior. In such materials, resistivity decreases at lower temperatures due to reduced phonon scattering. A higher RRR value indicates fewer impurities and defects, which reduce electron scattering. The TiN111 film exhibits the highest RRR value. This is consistent with its large grain size, which results in fewer defects at grain boundaries. The TiN200 film has an RRR value that is only slightly lower than that of the TiN111 film. This is somewhat surprising, as the TiN200 film has much smaller grains, which would typically lead to more dis-

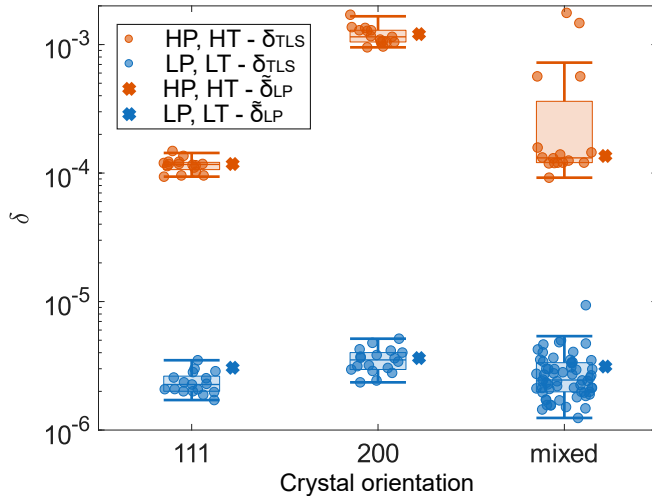


FIG. 8. δ_{TLS} and $\tilde{\delta}_{\text{LP}}$ for resonators structured from different TiN crystal orientations using the worst (HP+HT, red) and the best (LP+LT, blue) performing structuring methods tested.

order and increased scattering at grain boundaries. However, the high RRR value and the smaller resistivity suggests that the film is well-ordered within its volume, despite the smaller grain size. The mixed TiN film exhibits an RRR value substantially lower than the other two films. This indicates increased disorder that might be explained by different kinds of grain boundaries that occur between the two different grains. The T_c values of all the TiN films are in the region between 4.2 K and 5.2 K and therefore are only slightly lower than the bulk literature value of 5.8 K²⁸.

The TLS and LP losses of the three TiN films are demonstrated in Figure 8. For improved readability, only the median $\tilde{\delta}_{\text{LP}}$ of the LP losses are shown. The box plot visualizes data from single resonators as circles and the box and the bars visualize the interquartile range (IQR) with outliers above 1.5*IQR. We compare the HP/HT and LP/LT process combinations, chosen to represent the extremes: the LP etch with LT strip, which yields the best performance with $\tilde{\delta}_{\text{LP}}$ and δ_{TLS} approaching 10^{-6} , and the HP etch with HP strip, which yields the worst performance with both losses two to three orders of magnitude higher. Details about the influence of the etching will follow below.

The TiN200 films generally exhibit higher losses compared to the TiN111 films, particularly for the HP/HT process combinations. The TiNmixed film demonstrates a median TLS loss $\tilde{\delta}_{\text{TLS}}$ comparable to that of the TiN111 films, but its data points span the range observed for both TiN111 and TiN200. This trend is consistent across both structuring methods. The inferior performance of the TiN200 films may be attributed to their smaller grain sizes relative to the TiN111 films. Smaller grain sizes result in more grain boundaries, which are prone for oxidation. As oxides are known TLS hosts^{19,24,29-34} this is expected to contribute to increased losses. This hypothesis is supported by the lower RRR value observed for the TiN200 films. It remains unclear why most resonators fabricated from the TiNmixed films perform similarly to those made from

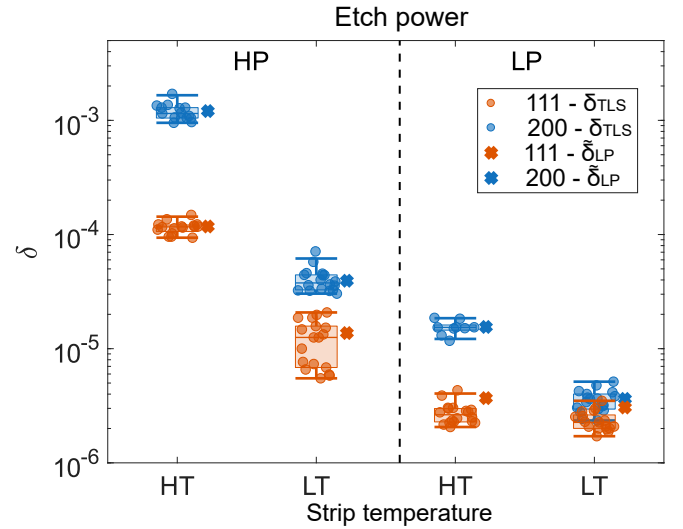


FIG. 9. δ_{TLS} and $\tilde{\delta}_{\text{LP}}$ for TiN111 (red) and TiN200 (blue) resonators with different etch recipes (top) and strip temperatures (bottom).

TiN111, despite the presence of grains with both orientations and possibly amorphous regions. However, XRD data indicate that the grain sizes in the TiNmixed films are larger than those in the TiN200 films. This observation may explain the generally better performance of the TiNmixed films and supports the hypothesis that grain boundaries significantly contribute to losses. Resonators of the TiNmixed films that incorporate more grain boundaries by chance therefore perform as worse as the TiN200 resonators.

2. Influence of structuring processes

The focus now shifts to examining the influence of the structuring processes on the TLS and LP loss of the respective resonators. For this purpose, Figure 9 summarizes δ_{TLS} for all four process combinations derived from pairing LP and HP etching with LT and HT resist stripping. The median for both, TLS and LP losses, are comparable for the respective process parameters. As TiNmixed films are expected to exhibit behavior consistent with the trends described earlier, they are excluded from the discussion in this section. Only the values for TiN200 and TiN111 films are shown. The generally better performance of the TiN111 films compared to the TiN200 films, as described above, is also confirmed in this graph. Since the Si substrates used are well-defined high-ohmic wafers, the dielectric substrate loss δ_{Si} remains constant across all process variations under discussion. Additionally, given the high uniformity and reproducibility of the TiN deposition processes, as described in Section III A 1, we can assume that the TLS loss at the MS interface also remains constant within each deposition process. It should be noted that for small overetch depths in the range of 0–100 nm, the participation ratios of our designs do not change substantially, as shown in Table IV. They decrease slightly with increasing overetch depth, as the electric field moves further away from

lossy regions.

a. Dry etching According to the point just made the HP etch, which introduces overetching into the silicon, should, if anything, result in lower losses. However, it is a clear result of this study that the HP etch generally introduces more losses into the system than the LP etch. This is the case for all four tested parameter variations. This etch process influences two interfaces: the SA interface and the MA interface, but the MA interface only in the small region of the sidewall. Distinguishing between these two effects is not possible with the current setup.

The SA interface of the HP etching is rougher than that of the LP etching, as confirmed by the AFM measurements above. Additionally, the higher bias voltage in the HP etching might lead to stronger amorphization of the Si surface due to bombardment by accelerated ions. Rougher surfaces, as well as amorphous silicon, are prone to increased oxidation, and it is known that amorphous silicon exhibits higher dielectric loss than crystalline silicon^{35–37}. To check whether the process conditions for the HP etch result in the implantation of boron into the Si surface⁷, a vapor phase decomposition (VPD) analysis of the Si surface was performed. However, the surface boron concentrations found for the HP process ($4.1 \cdot 10^{10} \text{ cm}^{-2}$) and the LP process ($10.6 \cdot 10^{10} \text{ cm}^{-2}$) are lower compared to the values for untreated silicon ($50.3 \cdot 10^{10} \text{ cm}^{-2}$).

The increase in Si surface roughness is known to be minimal, whereas the difference in the appearance of the etched sidewall is pronounced, as illustrated in Figure 6. This observation necessitates a discussion on the possibility that the inferior performance of the HP etch is not (only) due to an alteration of the Si surface but (in addition) strongly linked to its altered sidewall profile. The SEM image in Figure 6 shows that the surface area of the LP-etched sidewall is much rougher compared to that of the HP etch. The roughness was previously linked to different chemical etch rates for grain boundaries and TiN grains. This implies that the LP etch tends to stop at existing grain boundaries, while the HP etch exposes "bulk" TiN. This freshly exposed bulk TiN might develop a lossier oxide than the one at the grain boundaries. Another possible explanation is that the HP etch results in more lossy etch polymer residues on the sidewalls of the TiN, which are not fully removed by subsequent treatments.

b. Resist stripping Figure 9 clearly shows that the LT strip process results in lower losses compared to the HT strip process, consistently across all four process combinations. This processing step, being an H₂O vapor plasma step, influences only the SA and MA interfaces. As described in Section III A 2, the HT strip process is associated with the growth of thicker oxide layers on these interfaces, which explains the worse performance of the respective resonators

In summary, we have confirmed that all processing steps that favor oxidation lead to an increase in losses and we were able to link these processes to the associated oxide growth. For metal layers, grain boundaries are suspected to contribute to increased losses, as they promote oxide growth more effectively than a closed layer. Etched sidewalls also

contribute to losses through the oxidation of freshly etched surfaces. High-temperature processing in oxygen-containing atmospheres further enhances oxide growth, as observed in the HT resist strip processes. Additionally, amorphization, the presence of etch polymers on etched surfaces, and rough surfaces are also suspected to contribute to increased losses.

These contributions are difficult to distinguish. However, when considering the overall evidence, we can draw some conclusions. The TiN200 films suffer more from processing steps that promote oxidation compared to the TiN111 films. This indicates that TiN200 is less robust against oxidation. This hypothesis is further supported by the observation that the difference in losses between the HT and LT strip processes for the TiN200 films is much larger than for the TiN111 films. Most resonators made from TiNmixed films perform similarly to those made from TiN111 films, despite the smaller grain size of the TiNmixed films compared to the TiN111 films. This suggests that the worse performance of the TiN200 films is also not (only) due to its decreased grain size. Rather, the TiN200 orientation seems to provide a surface that is more prone to developing a lossier oxide compared to the TiN111 orientation. Another explanatory approach for the poor performance of the TiN200 films might be that the deposition process generates a thicker MS region, which contributes more to the losses. However, this explanation can be ruled out, as the TLS and LP losses of the exact same film are minimal when the LP etch is combined with the LP strip process, and neither of these processes alters the MS region. All in all, this set of experiments demonstrates that, although the MS interface has the largest participation ratio, the lossy surface oxides at the SA and MA interfaces make these two regions the dominant loss channels. This is supported by the fact that the etch and strip processes exclusively affect these two interfaces, resulting in noticeably different amounts of loss. This distinction becomes particularly clear when comparing the HP/HT resonators with the LP/LT resonators. For the LP/LT resonators, the losses originating from the SA and MA regions are substantially reduced, suggesting that the dominant loss channel may now shift to the MS interface. It can be inferred that the majority of the contribution to the losses originates from the MA interface region, as the Si interface for the four process combinations under investigation so far undergoes hardly any changes.

3. Influence of BOE wet etching and time coupling

The final experimental series investigates the post-treatment with a wet etch using BOE and its effect on the loss tangents. Since the TiNmixed films tend to span the range of quality factors expected for TiN111 and TiN200 films, this experiment was conducted exclusively with TiNmixed films. The process combinations used were the best-performing combination (LP etch and LT strip) and the worst-performing combination (HP etch and HT strip), as in previous experiments. As both native oxides (from silicon and TiN) can be etched with BOE, this processing step affects both the

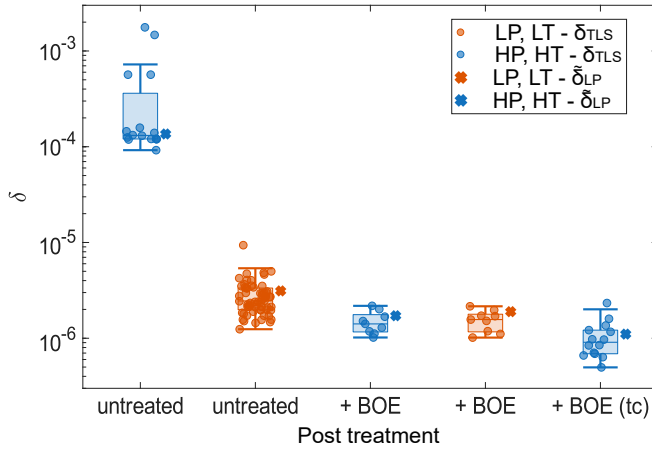


FIG. 10. Influence of BOE treatment on δ_{TLS} and $\tilde{\delta}_{\text{LP}}$ of HP+HT (blue) and LP+LT (red) manufactured TiNmixed samples and in combination with 2 hour timecoupling (tc) between measurements and cooldown.

SA and MA interfaces. For the MA interface, it is important to note that both the etched sidewall and the top surface are impacted. Since this processing step affects all interfaces exposed to air, it is challenging to separate the individual contributions of each interface to the overall losses. The results of the experiment, where resonators made from TiNmixed films were BOE-etched and then the same films were remeasured, are shown in Figure 10. Both samples were cooled down within one day after etching, while an additional sample, etched with HP and stripped with HT, was cooled down approximately two hours after BOE etching (tc). Although the two structuring procedures under investigation initially exhibit δ_{TLS} and $\tilde{\delta}_{\text{LP}}$ values that differ by approximately two orders of magnitude, the same two samples, after BOE etching, converge to the same loss level, regardless of the stripping or etching process used beforehand. Time coupling further reduced δ_{TLS} to $9.67 \cdot 10^{-7}$ and $\tilde{\delta}_{\text{LP}}$ to $11.04 \cdot 10^{-7}$. This result aligns with the hypothesis described earlier, suggesting that the losses introduced by the HP etch or HT strip processes can be attributed to lossy oxides at the SA and MA interfaces, including oxidation at grain boundaries. The small difference observed between the 2-hour and 24-hour delays after BOE treatment indicates that reoxidation at room temperature saturates quickly. No substantial additional oxide growth occurs between 2 and 24 hours after BOE treatment. Additional oxide growth can mainly be achieved through heating in an oxygen-containing atmosphere or oxygen plasma treatment, as it occurs during the LT resist stripping and, to a much greater extent, during the HT resist stripping.

IV. CONCLUSION

A comprehensive experimental study was conducted to analyze the dielectric losses of TiN resonators, involving three deposition processes, two etch processes, and two resist strip processes. Specifically, we achieved two distinct polycrys-

talline TiN depositions with exclusively (111) and (200) in-plane orientations, as well as a mixed deposition combining both. These orientations were verified using XRD. Resonators structured from the different TiN films exhibited similar minimal TLS and LP losses, with TiN111 yielding the lowest median losses. Additionally, TiN111 demonstrated greater robustness against reoxidation compared to TiN200 and TiN-mixed films. In contrast to the different TiN films, the applied etch and resist strip process have far greater influence on the measured δ_{TLS} and $\tilde{\delta}_{\text{LP}}$. Overall, the LP etch process combined with a LP resist strip exhibit the lowest losses independent of the crystal orientation. By leaving the participation ratios almost constant and comparing the different process combinations using structural analysis as well as cryogenic characterization methods we were able to locate the limiting losses introduced by processes that favor the growth of oxides on the MA and SA interfaces. This hypothesis could be confirmed with BOE post treatment that removed the oxides grown during these steps and renders unimportant which etching and resist stripping process was used beforehand. This marks the BOE post treatment as a beneficial approach to remove TLS losses induced by the structuring process. Ensuring that the measured losses are not dominated by the structuring method is crucial for accurate characterization, especially when wanting to isolate the impact of superconducting layer properties on the dielectric losses of resonators. Therefore, combining the BOE dip with time coupled measurements was shown to yield the lowest median TLS loss with $\tilde{\delta}_{\text{TLS}} = 9.67 \cdot 10^{-7}$ and LP loss with $\tilde{\delta}_{\text{LP}} = 11.04 \cdot 10^{-7}$ in this study approaching an internal quality factor of one million on par with those reported in the literature⁸. Collectively, our broad study using different TiN crystal orientations and structuring processes provides insight into critical process steps of an industry-grade 200 mm CMOS-compatible resonator workflow used for qubit fabrication.

ACKNOWLEDGMENTS

The authors gratefully acknowledge the support of TUM CRC for assistance with XRD measurements and extend their thanks to Felix Rucker, Sabrina Kressierer, and Oscar Gargiulo from kiutra GmbH for insightful discussions regarding cryogenic measurements. Special thanks are due to Dr. Lars Nebrich for his valuable support with layout design. The authors also express their gratitude to M. Hahn and M. König for their contributions and constructive discussions during process development. Finally, the authors thank the entire Fraunhofer EMFT cleanroom staff for their expertise and dedication in ensuring high-quality fabrication.

This work was funded by the Munich Quantum Valley (MQV) – Consortium Scalable Hardware and Systems Engineering (SHARE), funded by the Bavarian State Government with funds from the Hightech Agenda Bavaria, the Munich Quantum Valley Quantum Computer Demonstrator - Superconducting Qubits (MUNIQC-SC) 13N16188, funded by the Federal Ministry of Education and Research, Germany, and the Open Superconducting Quantum Computers (Open-

SuperQPlus) Project - European Quantum Technology Flagship.

DATA AVAILABILITY STATEMENT

The data that support the findings of this study are available from the corresponding author upon reasonable request.

- ¹A. G. Fowler, M. Mariantoni, J. M. Martinis, and A. N. Cleland, *Phys. Rev. A* **86**, 032324 (2012).
- ²L. K. Grover, *Phys. Rev. Lett.* **79**, 325 (1997).
- ³D. R. W. Yost, M. E. Schwartz, J. Mallek, D. Rosenberg, C. Stull, and et.al., *npj Quantum Information* **6**, 59 (2020).
- ⁴F. Arute, K. Arya, R. Babbush, D. Bacon, J. C. Bardin, and et.al., *Nature* **574**, 505 (2019).
- ⁵J. Gao, M. Daal, A. Vayonakis, S. Kumar, J. Zmuidzinas, B. Sadoulet, B. A. Mazin, P. K. Day, and H. G. Leduc, *Applied Physics Letters* **92**, 152505 (2008).
- ⁶B. Schoof, M. Singer, S. Lang, H. Gupta, D. Zahn, J. Weber, and M. Tornow, in *2024 IEEE International Conference on Quantum Computing and Engineering (QCE)* (IEEE Computer Society, Los Alamitos, CA, USA, 2024) pp. 1228–1232.
- ⁷M. Sandberg, M. R. Vissers, J. S. Kline, M. Weides, J. Gao, D. S. Wisbey, and D. P. Pappas, *Applied Physics Letters* **100**, 262605 (2012).
- ⁸M. R. Vissers, J. Gao, D. S. Wisbey, D. A. Hite, C. C. Tsuei, A. D. Corcoles, M. Steffen, and D. P. Pappas, *Applied Physics Letters* **97**, 232509 (2010).
- ⁹S. Ohya, B. Chiaro, A. Megrant, C. Neill, R. Barends, Y. Chen, J. Kelly, D. Low, J. Mutus, P. J. J. O'Malley, P. Roushan, D. Sank, A. Vainsencher, J. Wenner, T. C. White, Y. Yin, B. D. Schultz, C. J. Palmström, B. A. Mazin, A. N. Cleland, and J. M. Martinis, *Supercond. Sci. Technol.* **27**, 015009 (2014).
- ¹⁰J. B. Chang, M. R. Vissers, A. D. Córcoles, M. Sandberg, J. Gao, D. W. Abraham, J. M. Chow, J. M. Gambetta, M. Beth Rothwell, G. A. Keefe, M. Steffen, and D. P. Pappas, *Applied Physics Letters* **103**, 012602 (2013).
- ¹¹G. Calusine, A. Melville, W. Woods, R. Das, C. Stull, V. Bolkhovskiy, D. Braje, D. Hover, D. K. Kim, X. Miloshi, D. Rosenberg, A. Sevi, J. L. Yoder, E. Dauler, and W. D. Oliver, *Applied Physics Letters* **112**, 062601 (2018).
- ¹²K. R. Amin, C. Ladner, G. Jourdan, S. Hentz, N. Roch, and J. Renard, *Applied Physics Letters* **120**, 164001 (2022).
- ¹³J. M. Martinis, *Quantum Inf Process* **8**, 81 (2009).
- ¹⁴G. F. Harrington and J. Santiso, *J Electroceram* **47**, 141 (2021).
- ¹⁵R. N. Simons, *Coplanar Waveguide Circuits, Components, and Systems*, 1st ed. (Wiley, 2001).
- ¹⁶M. Göppl, A. Fragner, M. Baur, R. Bianchetti, S. Filipp, J. M. Fink, P. J. Leek, G. Puebla, L. Steffen, and A. Wallraff, *Journal of Applied Physics* **104**, 113904 (2008).
- ¹⁷S. Probst, F. B. Song, P. A. Bushev, A. V. Ustinov, and M. Weides, *Review of Scientific Instruments* **86**, 024706 (2015).
- ¹⁸A. Bruno, G. de Lange, S. Asaad, K. L. van der Enden, N. K. Langford, and L. DiCarlo, *Applied Physics Letters* **106**, 182601 (2015).
- ¹⁹C. Müller, J. H. Cole, and J. Lisenfeld, *Rep. Prog. Phys.* **82**, 124501 (2019).
- ²⁰J. M. Martinis, K. B. Cooper, R. McDermott, M. Steffen, M. Ansmann, K. D. Osborn, K. Cicak, S. Oh, D. P. Pappas, R. W. Simmonds, and C. C. Yu, *Phys. Rev. Lett.* **95**, 210503 (2005).
- ²¹C. Wang, C. Axline, Y. Y. Gao, T. Brecht, Y. Chu, L. Frunzio, M. H. Devoret, and R. J. Schoelkopf, *Applied Physics Letters* **107**, 162601 (2015).
- ²²S. Ganjam, Y. Wang, Y. Lu, A. Banerjee, C. U. Lei, L. Krayzman, K. Kisslinger, C. Zhou, R. Li, Y. Jia, M. Liu, L. Frunzio, and R. J. Schoelkopf, *Nature Communications* **15**, 3687 (2024).
- ²³J. Wenner, R. Barends, R. C. Bialczak, Y. Chen, J. Kelly, E. Lucero, M. Mariantoni, A. Megrant, P. J. J. O'Malley, D. Sank, A. Vainsencher, H. Wang, T. C. White, Y. Yin, J. Zhao, A. N. Cleland, and J. M. Martinis, *Applied Physics Letters* **99**, 113513 (2011).
- ²⁴W. Woods, G. Calusine, A. Melville, A. Sevi, E. Golden, D. Kim, D. Rosenberg, J. Yoder, and W. Oliver, *Phys. Rev. Appl.* **12**, 014012 (2019), publisher: American Physical Society.
- ²⁵International Centre for Diffraction Data, "Powder Diffraction File® Card No. 00-038-1420 for Titanium Nitride (TiN)," <https://www.icdd.com/> (2018), standard reference pattern for face-centered cubic TiN used in XRD phase identification.
- ²⁶S. Ohya, B. Chiaro, A. Megrant, C. Neill, R. Barends, Y. Chen, J. Kelly, D. Low, J. Mutus, P. O'Malley, P. Roushan, D. Sank, A. Vainsencher, J. Wenner, T. C. White, Y. Yin, B. D. Schultz, C. J. Palmström, B. A. Mazin, A. N. Cleland, and J. M. Martinis, "Sputtered tin films for superconducting coplanar waveguide resonators," (2013), arXiv:1306.2966 [cond-mat.suprcon].
- ²⁷H.-Y. Chen and F.-H. Lu, *Journal of Vacuum Science & Technology A: Vacuum, Surfaces, and Films* **23**, 1006 (2005).
- ²⁸J. R. Rumble, ed., *CRC Handbook of Chemistry and Physics*, 103rd ed. (CRC Press, 2022) internet version 2021 = 103rd print edition.
- ²⁹A. D. O'Connell, M. Ansmann, R. C. Bialczak, M. Hofheinz, N. Katz, E. Lucero, C. McKenney, M. Neeley, H. Wang, E. M. Weig, A. N. Cleland, and J. M. Martinis, *Applied Physics Letters* **92**, 112903 (2008).
- ³⁰M. V. P. Altoé, A. Banerjee, C. Berk, A. Hajr, A. Schwartzberg, C. Song, M. Alghadeer, S. Aloni, M. J. Elowson, J. M. Kreikebaum, E. K. Wong, S. M. Griffin, S. Rao, A. Weber-Bargioni, A. M. Minor, D. I. Santiago, S. Cabrini, I. Siddiqi, and D. F. Ogletree, *PRX Quantum* **3**, 020312 (2022).
- ³¹R. D. Chang, N. Shumiya, R. A. McLellan, Y. Zhang, M. P. Bland, F. Bahrami, J. Mun, C. Zhou, K. Kisslinger, G. Cheng, B. M. Smitham, A. C. Pakpour-Tabrizi, N. Yao, Y. Zhu, M. Liu, R. J. Cava, S. Gopalakrishnan, A. A. Houck, and N. P. de Leon, *Phys. Rev. Lett.* **134**, 097001 (2025), publisher: American Physical Society.
- ³²J. Verjauw, A. Potočnik, M. Mongillo, R. Acharya, F. Mohiyaddin, G. Simion, A. Pacco, T. Ivanov, D. Wan, A. Vanleenhove, L. Souriau, J. Jusot, A. Thiam, J. Swerts, X. Piao, S. Couet, M. Heyns, B. Govoreanu, and I. Radu, *Phys. Rev. Appl.* **16**, 014018 (2021), publisher: American Physical Society.
- ³³J. Biznárová, A. Osman, E. Rehnman, L. Chayanun, C. Križan, P. Malmberg, M. Rommel, C. Warren, P. Delsing, A. Yurgens, J. Bylander, and A. Fadavi Roudsari, *npj Quantum Information* **10**, 78 (2024).
- ³⁴H. Gupta, R. Pereira, L. Koch, N. Bruckmoser, M. Singer, B. Schoof, M. Kompatscher, S. Filipp, and M. Tornow, *Communications Materials* **7**, 58 (2026).
- ³⁵C. M. Quintana, A. Megrant, Z. Chen, A. Dunsworth, B. Chiaro, R. Barends, B. Campbell, Y. Chen, I.-C. Hoi, E. Jeffrey, J. Kelly, J. Y. Mutus, P. J. J. O'Malley, C. Neill, P. Roushan, D. Sank, A. Vainsencher, J. Wenner, T. C. White, A. N. Cleland, and J. M. Martinis, *Applied Physics Letters* **105**, 062601 (2014).
- ³⁶A. Dunsworth, A. Megrant, C. Quintana, Z. Chen, R. Barends, B. Burkett, B. Foxen, Y. Chen, B. Chiaro, A. Fowler, R. Graff, E. Jeffrey, J. Kelly, E. Lucero, J. Y. Mutus, M. Neeley, C. Neill, P. Roushan, D. Sank, A. Vainsencher, J. Wenner, T. C. White, and J. M. Martinis, *Applied Physics Letters* **111**, 022601 (2017).
- ³⁷C. E. Murray, *Materials Science and Engineering: R: Reports* **146**, 100646 (2021).